SCIENCE CHINA
Chemistry

•ARTICLES•

July 2022 Vol.65 No.7: 1347–1355
https://doi.org/10.1007/s11426-022-1249-7

Efficient circularly polarized photoluminescence and electroluminescence of chiral spiro-skeleton-based thermally activated delayed fluorescence molecules

Yi-Pin Zhang[1], Shi-Quan Song[1], Meng-Xi Mao[1], Cheng-Hui Li[1], You-Xuan Zheng[1,2*] & Jing-Lin Zuo[1]

, corrected publication 2022

[1]*State Key Laboratory of Coordination Chemistry, Jiangsu Key Laboratory of Advanced Organic Materials, School of Chemistry and Chemical Engineering, Nanjing University, Nanjing 210023, China;*
[2]*MaAnShan High-Tech Research Institute of Nanjing University, Maanshan 238200, China*

Received March 24, 2022; accepted April 08, 2022; published online May 20, 2022

Chiral thermally activated delayed fluorescence (TADF) molecules showing circularly polarized luminescence (CPL) have great potential in 3D displays. However, the relationships among CPL property, device performance and molecule structure are still not clear. In this article, we develop a strategy to promote dissymmetry factors without sacrifice in device performance and study the impact of molecule structures towards CPL property. Three novel TADF enantiomers are synthesized and studied. (*R*/*S*)-SCN with diminutive cyano group as an acceptor shows dissymmetry factor $|g_{PL}| \approx 1.4\times10^{-3}$ and noticeable organic light-emitting diode (OLED) performances with a maximum external quantum efficiency (EQE_{max}) of 23.0%. For (*R*/*S*)-SPHCN, the prolonged electron withdrawing group benzonitrile enhances $|g_{PL}|$ up to 3.6×10^{-3} with decreased device EQE_{max} of 15.4%. By further replacing benzonitrile with (trifluoromethyl)pyridine, the enantiomers of (*R*/*S*)-SCFPY show similar $|g_{PL}|$ factors of 3.5×10^{-3} and device EQE_{max} up to 23.3%, which represents the highest efficiency among sprio-type TADF materials based OLEDs. Furthermore, the OLEDs also show obvious circularly polarized electroluminescence with g_{EL} factors of $-1.4/1.8\times10^{-3}$, $-3.6/3.6\times10^{-3}$ and $-3.7/3.6\times10^{-3}$, respectively. These results indecate by delicate functional group engineering, high *g* factor can be achieved while maintaining decent device performances. Besides, (*R*/*S*)-SCFPY represents an impressive TADF emitter, which shows promoted *g* factor and recorded high device EQE_{max} among similar molecules.

chiral spiro-skeleton, thermally activated delayed fluorescence, circularly polarized photoluminescence, circularly polarized electroluminescence, dissymmetry factor

Citation: Zhang YP, Song SQ, Mao MX, Li CH, Zheng YX, Zuo JL. Efficient circularly polarized photoluminescence and electroluminescence of chiral spiro-skeleton-based thermally activated delayed fluorescence molecules. *Sci China Chem*, 2022, 65: 1347–1355, https://doi.org/10.1007/s11426-022-1249-7

1 Introduction

Chiral materials with circularly polarized luminescence (CPL) property are important components of a variety of technology, including biological sensing, data storage and next-generation 3D displays [1]. Among them, the circularly polarized organic light emitting diodes (CP-OLEDs) featuring a direct generation of CP-electroluminescence (CPEL) can avoid the decreased brightness and efficiency loss through polaroids, suggesting their potential application in 3D displays. Thus, the development of CP-OLEDs has become a cutting-edge topic in both academia and industry [2]. It is well-known that OLEDs contain a stacked device structure. Thus, to achieve CPEL, the key point is to develop chiral luminescent materials and construct a CP-emissive layer. Up to now, three types of luminescent materials have

*Corresponding author (email: yxzheng@nju.edu.cn)

© Science China Press and Springer-Verlag GmbH Germany, part of Springer Nature 2022, corrected publication 2022

been successfully applied in CP-OLEDs including chiral fluorescent, phosphorescent and thermally activated delayed fluorescence (TADF) materials [3]. Among these materials, chiral TADF materials receive the most attention due to their ability to harvest both singlet and triplet excitons *via* the reverse intersystem crossing (RISC) process without the involvement of noble metal. Thus, chiral TADF materials are now considered as the state-of-the-art materials for CP-OLEDs [4].

Since the first report of chiral TADF materials-based CP-OLEDs by Pieters's group [5] in 2016, remarkable progress has been made in this area. So far, three strategies have been proposed to construct CP-TADF molecules, including chiral perturbation, chiral connection and chiral luminescence center strategy. Chiral perturbation refers to the linkage of the chiral unit to TADF core, including binaphthol, octahydro-binaphthol and paracyclophane skeleton [6–16], *etc*. Chiral connection indicates the connection of several TADF active units *via* the chiral linker, which mainly contains skeletons such as biphenyl, 1,2-diaminocyclohexane, quaternary carbon atom and triptycene [17–27]. The chiral luminescence center strategy means the installation of donor and acceptor units onto a chiral framework resulting in asymmetrically distributed highest occupied molecular orbitals (HOMOs) and lowest unoccupied molecular orbitals (LUMOs) [28–35]. Benefitted from the continuous efforts of the researchers, TADF materials-based CP-OLEDs have shown noticeable device performances with a maximum external quantum efficiency (EQE_{max}) up to 20.0% [30], 32.6% [7], and 20.3% [16] for blue, green, and orange-red emissions, respectively.

However, almost all chiral TADF molecules show low dissymmetry factors (g) around 10^{-4}–10^{-3} order of magnitudes at the present stage. Theoretically, CPL performance could be calculated by the equation $g_{lum}=4\times(|\mu_e|\cdot|\mu_m|\cdot\cos\theta)/(|\mu_e|^2+|\mu_m|^2)$, where μ_e, μ_m and θ denote electric transition dipole moments, magnetic transition dipole moments and their spatial angle, respectively. Experimentally, the g factors are measured according to the equation $g_{lum}=2\times(I_L-I_R)/(I_L+I_R)$, where I_L and I_R denote the luminescence intensity of left- and right-CPL, respectively [3]. Nevertheless, in terms of chiral TADF molecules, the calculated results could only give instruction on the level of the trend. The calculated g factors still show a large deviation from experimental results [12,24,34]. Currently, the relationship between the chemical structure of TADF molecule and CPL property remains unclear which hinders the promotion of CPL signals. Although a variety of TADF molecules have been developed, owing to the difficulty in molecule design and chiral separation, only a few reports focus on the impact of molecule structure on CPL property and device performance. In our previous study, the CPL property was enhanced by regulating the shape of molecules from rod to helix. However, sacrifice in device performances occurred along with amplification of g factors [34]. Thus, there is an urgent demand for a strategy to promote the CPL property of chiral TADF molecules while maintaining decent device performances.

In this study, promotion in both CPL property and device performances is achieved by delicate functional group engineering (Figure 1). Previously, we developed a pair of TADF enantiomers OSFSO with remarkable device performance [30]. Based on this work, we developed three pairs of novel spiro-type TADF enantiomers with similar chiral skeleton, spiro[quinolino[3,2,1-*kl*]phenoxazine-9,9′-thioxanthene]-2′-carbonitrile10′,10′-dioxide (SCN), 4-(10′,10′-dioxidospiro[quinolino[3,2,1-*kl*]phenoxazine-9,9′-thioxanthen]-2′-yl)benzonitrile (SPHCN) and 2′-(2-(trifluoromethyl) pyridin-4-yl) spiro[quinolino [3,2,1-*kl*] phenoxazine-9,9′-thioxanthene] 10′,10′-dioxide (SCFPY), respectively. By comparing their chiroptical properties and device performances, we disclosed that g factors can be enhanced by prolonging the length of acceptor units. The three pairs of TADF enantiomers share the same phenoxazine donors, but with different acceptors. SCN possessing a localized cyano group as an acceptor shows $|g_{PL}| \approx 1.4\times10^{-3}$, SPHCN containing benzonitrile as a prolonged acceptor exhibits $|g_{PL}| \approx 3.6\times10^{-3}$, and 2-(trifluoromethyl)pyridine used as a prolonged acceptor unit for SCFPY results in $|g_{PL}|$

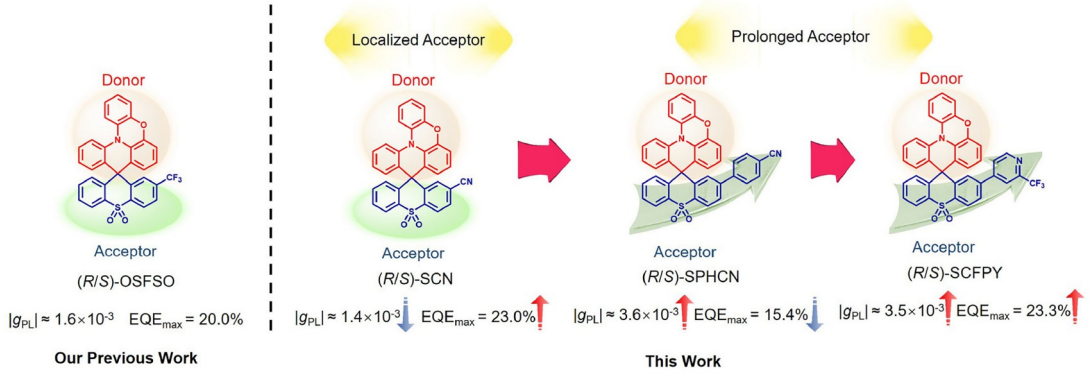

Figure 1 Illustration of our previous work and chiral TADF materials studied in this work (color online).

$\approx 3.5\times10^{-3}$. Theoretical calculation results indicate that the enhanced CPL property may be attributed to the decrease in spatial angle between electric and magnetic transition dipole moments. As for corresponding OLEDs, SPHCN shows medium performances with an EQE_{max} of 15.4%. Meanwhile, SCN and SCFPY show decent device performances with EQE_{max} values of 23.0% and 23.3%, respectively, and the EQE of 23.3% represents a remarkable spiro-type TADF material [30,36–45]. Furthermore, the CP-OLEDs also show obvious CP-electroluminescence with g_{EL} factors of $-1.4/1.8\times10^{-3}$, $-3.6/3.6\times10^{-3}$ and $-3.7/3.6\times10^{-3}$, respectively. These results indicate that by delicate functional group engineering, a high *g* factor and decent device performances can be compatible.

2 Experimental

All of the reagents and solvents were obtained from commercial sources and directly used without any further purification. The nuclear magnetic resonance (NMR) measurement was conducted on BRUKER AVANCE III 400 MHz spectrometer and BRUKER AVANCE III 600 MHz spectrometer (Germany). The high-resolution mass spectra were obtained by using the Bruker micrOTOF-Q III. The absorption and photoluminescence spectra were measured on a Shimadzu UV-3100 and a HORIBA Fluorolog-3 photoluminescence spectrophotometer (USA), respectively. The cyclic voltammetry measurements were conducted on a MPI-A multifunctional electrochemical and chemiluminescent system (Xi'an Remex Analytical Instrument Ltd. Co., China) at room temperature, with a polished Pt disk as the working electrode, platinum thread as the counter electrode and Ag-$AgNO_3$ (0.1 M) in CH_3CN as the reference electrode, *tetra-n*-butylammonium perchlorate (0.1 M) was used as the supporting electrolyte, respectively. Fc^+/Fc was used as the internal standard, the scan rate was 0.1 V/s. The absolute photoluminescence quantum yields *via* an integrating sphere and the decay lifetimes of the compounds were measured with HORIBA Fluorolog-3 fluorescence spectrometer (USA). The thermogravimetric analysis (TGA) curves were performed on a Pyris 1 DSC under nitrogen at a heating rate of 10 °C min^{-1}. The separation of enantiomers was conducted by chiral high performance liquid chromatography (HPLC). The circular dichroism (CD) spectra were measured on a Jasco J-810 circular dichroism spectrometer with "standard" sensitivity. The circularly polarized luminescence (CPL) spectra were measured on a Jasco CPL-300 spectrophotometer with "Standard" sensitivity at 100 nm/min scan speed and respond time of 4.0 s employing "slit" mode. The ground state calculations were based on the optimized structure using Gaussian 09 by density functional theory (DFT) with B3LYP functional and 6-31G(d) basis set. Excited state calculations were conducted by time-dependent density functional theory (TD-DFT) with B3LYP functional and 6-31G(d) basis set. Electric transition dipole moments, magnetic transition dipole moments were calculated with CAMB3LYP functional and 6-311G basis set. (Gaussian 09, Revision D.01, Gaussian, Inc., Wallingford CT, 2013) $|\mu_e|$ and $|\mu_m|$ were calculated *via* $\sqrt{x^2+y^2+z^2}$, where *x*, *y*, *z* denoted their component on three axes. $\cos\theta=(\mu_e\cdot\mu_m)/|\mu_e|\times|\mu_m|$, where μ_e and μ_m denoted vectors of electric transition dipole moments and magnetic transition dipole moments, respectively.

Indium-tin-oxide (ITO) coated glass with a sheet resistance of 10 Ω sq^{-1} was used as the anode substrate. Prior to film deposition, patterned ITO substrates were cleaned with detergent, washed with de-ionized water, dried and treated with oxygen plasma for 5 min at a pressure of 10 Pa to enhance the surface work function of ITO anode (from 4.7 to 5.1 eV). All the organic layers were deposited at the rate of 0.1 nm/s under a high vacuum ($\leq 2\times10^{-5}$ Pa). The doped layers were prepared by co-evaporating dopant and host material from two individual sources, and the doping concentrations were modulated by controlling the evaporation rate of the dopant. LiF and Al were deposited in another vacuum chamber ($\leq 8.0\times10^{-5}$ Pa) with the rates of 0.01 and 1 nm/s, respectively. The thicknesses of these deposited layers and the evaporation rate of individual materials were monitored in vacuum with quartz crystal monitors. A shadow mask was used to define the cathode and to make ten emitting dots (with an active area of 10 mm^2) on each substrate. Device performances were measured by using a programmable Keithley source measurement unit (Keithley 2400 and Keithley 2000) with a silicon photodiode. The EL spectra were measured with a HORIBA Fluorolog-3 spectrophotometer. Based on the uncorrected EL fluorescence spectra, the Commission Internationale de l'Eclairage (CIE) coordinates were calculated using the test program of Spectrascan PR650 spectrophotometer (USA). The EQE of EL devices was calculated based on the photo energy measured by the photodiode, the EL spectrum, and the current passing through the device.

3 Results and discussion

3.1 Synthesis and characterization

The detailed synthetic routes are listed in Supporting Information online The key intermediate 2′-bromospiro[quinolino [3,2,1-*kl*]phenoxazine-9,9′-thioxanthene]10′,10′-dioxide **6** could be synthesized *via* carbanion nucleophilic attack and dehydrated cyclization process from experimentally available starting materials. Considering the stable spiro-skeleton [46,47], HPLC with the chiral column was

employed to separate intermediate **6**. The conformation stability was confirmed by vacuum sublimation at 230 °C, and no racemization was observed (Figure S21, Table S1, Supporting Information online). TADF enantiomers SCN, SPHCN and SCFPY were synthesized *via* palladium catalyzed cyanation process and Suzuki coupling reaction from intermediate **6**. Based on mild reaction condition and full chirality transfer property of palladium catalyzed cross-coupling reaction, (*R*/*S*)-**6** was thereafter transferred to chiral TADF molecules (*R*/*S*)-SCN, (*R*/*S*)-SPHCN and (*R*/*S*)-SCFPY, the absolute configurations of (*R*/*S*)-SPHCN were also characterized *via* single crystal analysis (Figure 2, Table S2). Thermogravimetric analysis (TGA) curves demonstrated that all materials enjoy good thermostability with high decomposition temperatures (T_d, 5% loss of weight, Figures S22–S24) above 360 °C.

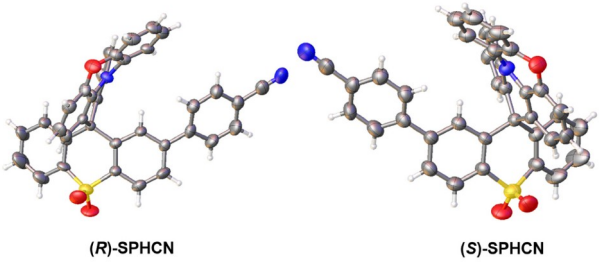

Figure 2 Single crystal structure of (*R*)-SPHCN and (*S*)-SPHCN (color online).

3.2 Theoretical calculation

To better gain insight into the properties of these enantiomers, DFT and TD-DFT calculations were conducted. Multiwfn 3.7 program was also employed to do relevant analysis [48]. As shown in Figure 3, for all TADF enantiomers, the HOMOs and LUMOs are well separated by the spiro-structure, with HOMOs located on the donor units and LUMOs lying on the acceptor units, which are the typical features of TADF molecules. For the three pairs of TADF molecules, HOMOs distribute rather averagely on phenoxazine and connected benzene rings, while LUMOs are attracted to one side of thioxanthenedioxide core. For SCN, the LUMOs mainly concentrate on the benzonitrile unit, while more delocalized LUMOs are observed for SPHCN and SCFPY owing to the prolonged acceptor components. From the single crystal structure of (*R*/*S*)-SPHCN (Figure 2), twisted configurations with perfect mirror symmetry can be observed. For both (*R*)-SPHCN and (*S*)-SPHCN, electron-donating phenoxazine units bend towards electron-withdrawing cyano benzene units, which is in line with the calculated results. Twisted conformation and electron cloud distribution for the three pairs of TADF molecules may help shorten the distance between HOMOs and LUMOs and promote their spatial interactions, which is in favor of through-space charge transfer (TSCT) process. The energy gaps (ΔE_{ST}) between singlet (S_1) and triplet (T_1) states are calculated to be around 0.01 eV for these enantiomers, which are small enough to facilitate an efficient TADF process.

As spiro-structure effectively cuts off the conjugation between donors and acceptors which shuts down the through-bond charge transfer channel (TBCT), the intramolecular charge transfer process mainly occurs *via* TSCT process which normally requires obvious intramolecular weak interactions [49]. Thus, the functions of reduced density gradient (RDG) and Sign $(\lambda_2)\rho$ are calculated to show the intramolecular non-covalent interactions in SCN, SPHCN and SCFPY and the results are listed in Figures S25–S27. From the RDG maps, the green region shows the presence of obvious interactions between donor and acceptor moieties as well as steric hindrance, which could be beneficial for TSCT process and reduce the energy loss of the excited molecules [50].

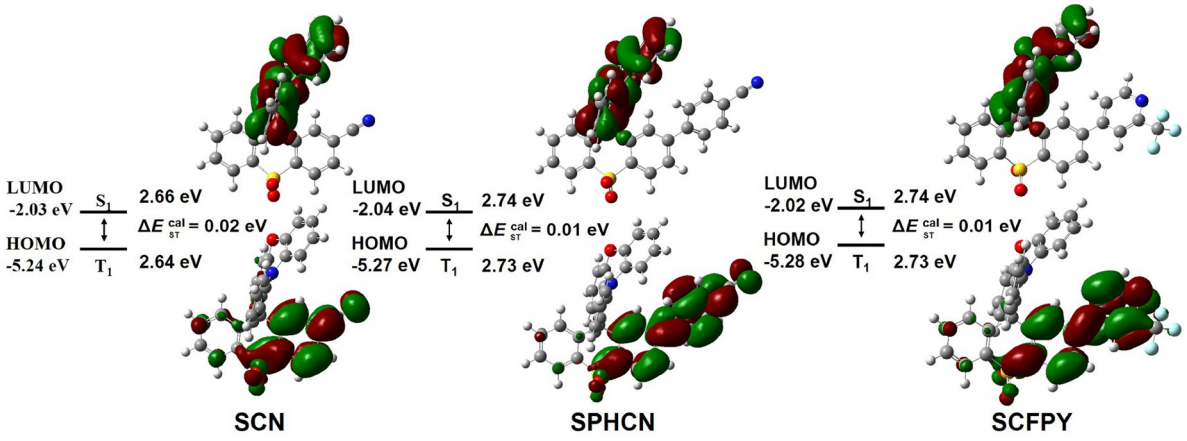

Figure 3 Calculated optimal structures, HOMO/LUMO distributions and energy levels of SCN, SPHCN and SCFPY (B3LYP functional with the 6-31G(d) basis set for DFT and TD-DFT calculation) (color online).

3.3 Electrochemical and photophysical property

Due to the almost identical properties of the enantiomers, (*rac*)-SCN, (*rac*)-SPHCN and (*rac*)-SCFPY were chosen as examples for investigating their electrochemical and photophysical properties. The electrochemical properties of the TADF molecules were measured in CH_3CN solution at room temperature with ferrocenium/ferrocene (Fc^+/Fc) as reference (Figures S28–S30). The HOMO energy levels were determined from the oxidation curve of cyclic voltammetry spectra, while LUMO levels were calculated according to the equation $E_{LUMO} = E_{HOMO} + E_g$, where E_g values were obtained from the onset of UV/Vis absorption spectra. The SCN, SPHCN and SCFPY displayed similar HOMO/LUMO energy levels with −5.31/−2.31, −5.30/−2.11 and −5.30/−2.19 eV, respectively.

As shown in the photoluminescence spectra (Figure 4), three TADF molecules exhibited green emission with λ_{max} of 522, 505 and 526 nm for SCN, SPHCN and SCFPY, respectively. As for absolute photoluminescence quantum yield (PLQY) and delayed fluorescence lifetime (τ_d) (Table 1, Figures S31–S36), obvious changes were observed for the three molecules. SCN and SCFPY showed high PLQYs up to around 89%, while SPHCN exhibited a medium PLQY of 67.4%. Furthermore, a rather long τ_d of 14.6 μs was observed for SPHCN. In contrast, relative short τ_ds of 2.1 and 1.6 μs were recorded for SCN and SCFPY, which would benefit their OLED performances. The differences between PLQY and τ_d can be attributed to the structure distinction of acceptor units. The plane conformation of benzonitrile may introduce more intramolecular rotation as well as intermolecular π-π interaction compared with the cyan group and branched 2-(trifluoromethyl)pyridine group, which may induce enhanced nonradiative transition and intermolecular quenching.

To verify the TADF property of the three molecules, several experiments were further conducted. From the solvent-depended UV/Vis absorption spectra and photoluminescence spectra, enhanced Stokes shift could be observed with the increase of solvent polarity (Figures S37–S39). SCN, SPHCN and SCFPY displayed red shifts of 159 nm (λ_{max} = 449 nm in hexane and λ_{max} = 608 nm in dichloromethane), 126 nm (λ_{max} = 441 in hexane and λ_{max} = 567 in dichloromethane) and 131 nm (λ_{max} = 461 hexane and λ_{max} = 592 in dichloromethane), respectively. However the UV/Vis absorption peaks of the three molecules remained almost the same. These phenomena indicated the obvious intramolecular CT state of the molecules. The energy gaps between S_1 and T_1 were estimated from the onset of the fluorescence and phosphorescence spectra at 77 K, and the ΔE_{ST} values were determined to be 0.01, 0.16 and 0.04 eV for SCN, SPHCN and SCFPY, anticipating fast RISC for efficient TADF process (Figures S40–S42). Thereafter, the oxygen quenching experiment and temperature-dependent

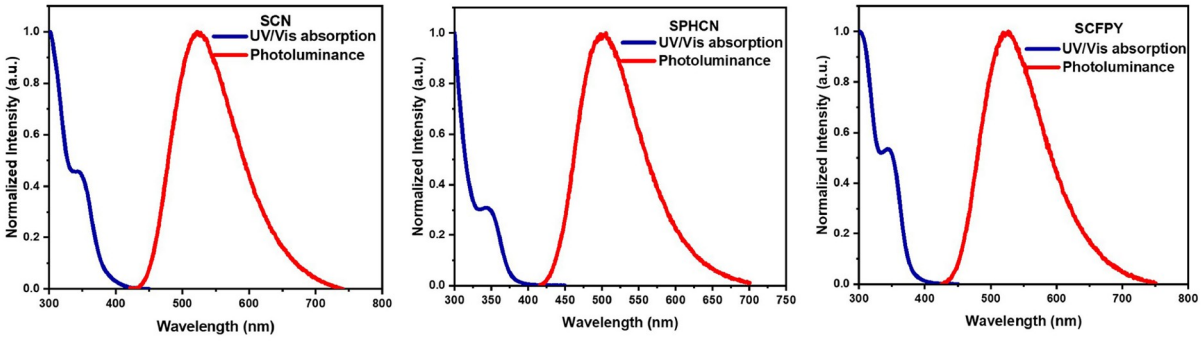

Figure 4 UV/Vis absorption and photoluminescence spectra (with excitation of 350 nm) of (*rac*)-SCN, (*rac*)-SPHCN and (*rac*)-SCFPY in toluene solution (color online).

Table 1 Collection of experimental data of SCN, SPHCN, SCFPY and previously reported OSFSO

Molecule	λ_{max} [a] (nm)	HOMO/LUMO [b] (eV)	ΔE_{ST} [c] (eV)	PLQY [d] (%)	τ_P [d] (ns)	τ_d [d] (μs)	T_d (°C)	g_{PL} [e] $\times 10^{-3}$
SCN	522	−5.31/−2.31	0.01	89.3	10	2.1	360	1.4/−1.3
SPHCN	505	−5.30/−2.11	0.16	67.4	16	14.6	396	3.5/−3.6
SCFPY	526	−5.30/−2.19	0.04	88.9	4	1.6	383	3.5/−3.5
OSFSO[f]	470	−5.35/−2.11	0.02	81.2	13.5	4.7	285	−1.6/1.4

a) Emission peak of fluorescence spectrum at room temperature in toluene solution. b) The HOMO energy level was determined from the oxidation curve of cyclic voltammetry, and the LUMO was calculated with the equation of $E_{LUMO}=E_{HOMO} + E_g$, where E_g was determined from the onset of UV/Vis absorption spectrum. c) Determined from the onset of the fluorescence and phosphorescence spectra at 77 K in toluene solution. d) Determined from co-doped film of 25 wt% dopant in 26DCzPPy. e) (*R*/*S*)-enantiomers measured in toluene solution at room temperature. f) Properties of previous reported TADF molecule OSFSO as a contrast.

transient photoluminescence measurements were also conducted to further prove TADF process. As shown in Figures S43–S45, microsecond scale delayed lifetime for the three molecules were observed from nitrogen saturated toluene solutions which could be quenched by bumping air. Considering the triplet state quenching ability of oxygen, T_1 state may be involved during the emission process, which is in line with the proposed RISC process. Moreover, from temperature-dependent transient lifetime curves of the three molecules, increased slopes were observed with the rise of temperature, which indicates an increased proportion of delayed components. This phenomenon further verifies the TADF nature of the designed molecules.

3.4 Chiroptical properties

Circular dichroism (CD) and CPL spectra were employed to characterize the chiroptical properties of the three pairs of enantiomers and the results were listed in Figure 5. In toluene solution, (*R*/*S*)-SCN, (*R*/*S*)-SPHCN and (*R*/*S*)-SCFPY exhibited perfect symmetrical CD spectra with obvious cotton effect in the range of 300–380 nm, and $|g_{abs}|$ was detected to be 9×10^{-4}, 8×10^{-4} and 7×10^{-4}, respectively. This indicated charity was successfully introduced into TADF molecules at the ground state. Meanwhile, almost symmetrical CPL spectra of these pairs of enantiomers were observed with *S*-configuration exhibiting positive signals and *R*-conformation displaying negative signals, respectively. For (*S*/*R*)-SCN, the photoluminescence dissymmetry factors (g_{PL}) were recorded to be $1.4/-1.3\times10^{-3}$, which are among the medium of reported chiral TADF molecules. Benefitted form the prolonged acceptor units, (*S*/*R*)-SPHCN and (*S*/*R*)-SCFPY showed twofold amplification of CPL signals with g_{PL} of $3.5/-3.6\times10^{-3}$ and $3.5/-3.5\times10^{-3}$, respectively. From these data, we observed that compared with SCN and OSFSO with short acceptor units, SPHCN and SCFPY with prolonged acceptor units showed a more than two-fold amplification of *g* factor. These results verified the feasibility of prolonging acceptor strategy, where CPL performance was two-fold enhanced without changing the chiral skeleton.

To further gain insight into the impact of prolonged acceptor units, theoretical calculations were conducted and the results were also listed in Figure 5. From theory, the *g* factors can be described as $g_{lum} \approx 4\times\left(|\mu_e|\cdot|\mu_m|\cdot\cos\theta\right)/\left(|\mu_e|^2+|\mu_m|^2\right)$. However, TADF molecules normally show small magnetic transition dipole moments with μ_m two-order-of-magnitudes lower than μ_e. Thus, the equation can be simplified as $g_{lum} \approx 4\times|\mu_m|\cdot\cos\theta/|\mu_e|$, where $|\mu_m|/|\mu_e|$ and $\cos\theta$ become the key factors to determine g_{lum}. In this study, (*S*)-SCN, (*S*)-SPHCN and (*S*)-SCFPY showed similar electronic and magnetic transition dipole moments with $|\mu_m| = 4.72\times10^{-21}$,

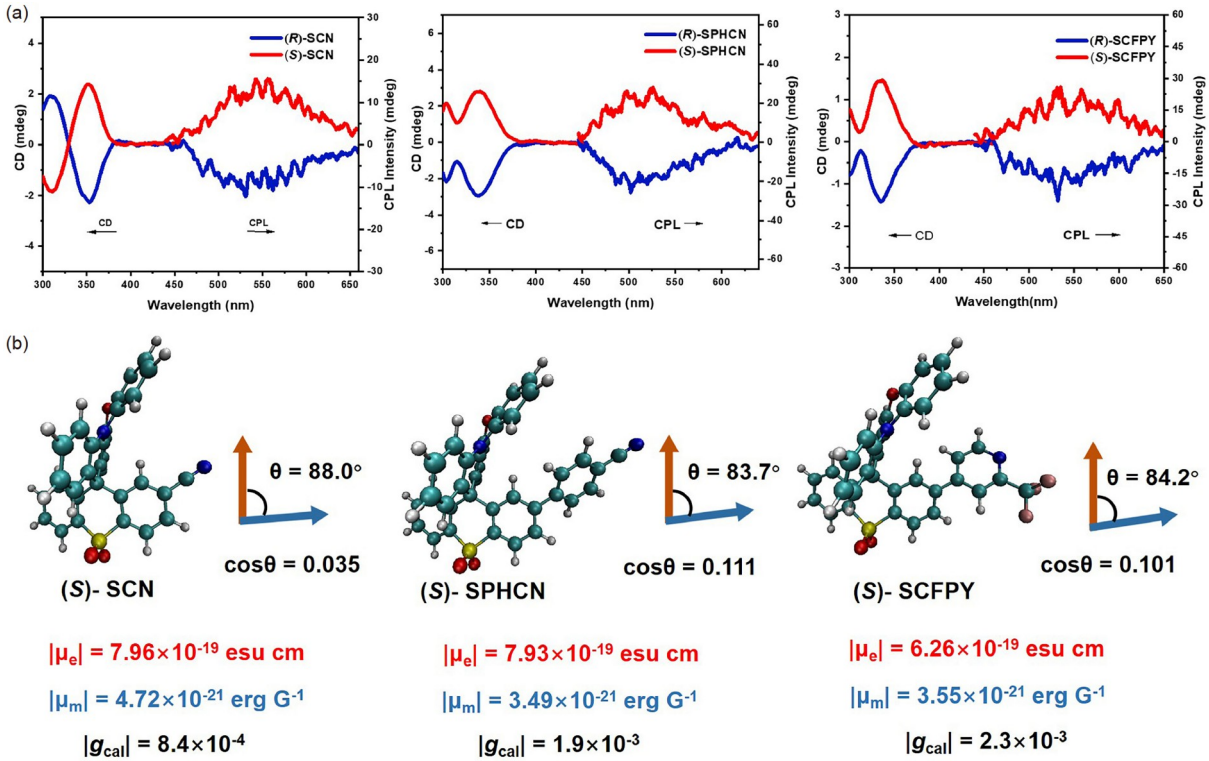

Figure 5 (a) CD and CPL spectra of SCN, SPHCN and SCFPY in toluene solutions; (b) calculated electric transition dipole moments, magnetic transition dipole moments and their spatial angle (CAMB3LYP functional with the 6-31G basis set for TD-DFT cauculation based on optimized structure) (color online).

3.49×10^{-21}, 3.55×10^{-21} esu cm and $|\mu_e|$ = 7.96×10^{-19}, 7.93×10^{-19} and 6.26×10^{-19} erg G^{-1}, respectively. However, angles between μ_m and μ_e varied obviously, and (*S*)-SCN showed $\theta \approx 88°$ while (*S*)-SPHCN and (*S*)-SCFPY displayed $\theta \approx 84°$, where about threefold amplification of cosθ was observed. As a result, (*S*)-SCN showed a calculated $|g_{cal}|$ factor of 8.4 $\times10^{-4}$, and (*S*)-SPHCN and (*S*)-SCFPY exhibited enhanced $|g_{cal}|$ factors of 1.9 $\times10^{-3}$ and 2.3 $\times10^{-3}$, respectively. Although the calculated data showed variations in experimental data, the trends were consistent. These results provided a theoretical basis for the functional group engineering strategy. Considering the influence of functional groups towards spiral angel between μ_m and μ_e, we suppose delicate regulation of the length of donor or acceptor units may be a feasible strategy to design chiral TADF materials with high dissymmetry factors and remarkable device performances.

3.5 OLED performance

Considering efficient TADF properties of the three molecules, they were employed as emitters for OLEDs. As shown in Figure 6, the optimal device followed such a structure: ITO/HATCN (hexa-azatriphenylene-hexacabonitrile) (10 nm)/TAPC (di-[4-(*N*,*N*-ditolyl-amino)phenyl]cyclohexane) (50 nm)/ emitters (25 wt%): 26DCzPPy (2,6-bis(3-(9*H*-carbazol-9-yl)pheninyl)pyridine) (20 nm)/TmPyPB (1,3,5-tri(m-pyrid-3-yl-phenyl)benzene) (50 nm)/LiF (1 nm)/Al (100 nm). Device with (*rac*)-SCN, (*rac*)-SPHCN and (*rac*)-SCFPY as emitters were named as **D1**, **D2** and **D3**, respectively. Device **D1** showed green emission centered at 519 nm with CIE coordinate of (0.34, 0.53), and the device displayed quite decent performances with an EQE_{max} of 23.0% and a maximum luminance (L_{max}) of 32,673 cd/m^2 (Table 2). Besides, **D1** showed rather a small efficiency roll-off with EQE of 14.7% at high luminance of 1,000 cd/m^2. **D2** exhibited green emission centered at 512 nm with CIE coordinate of (0.30, 0.52), but the EQE_{max} and L_{max} were lowered to 15.4% and 14,240 cd/m^2, respectively. The decrease in device performance could be attributed to the medium PLQY and rather large ΔE_{ST} of SPHCN which hindered TADF process. For device **D3**, maximum emission wavelength moved to 517 nm with CIE coordinate of (0.31, 0.51), the EQE_{max} reached

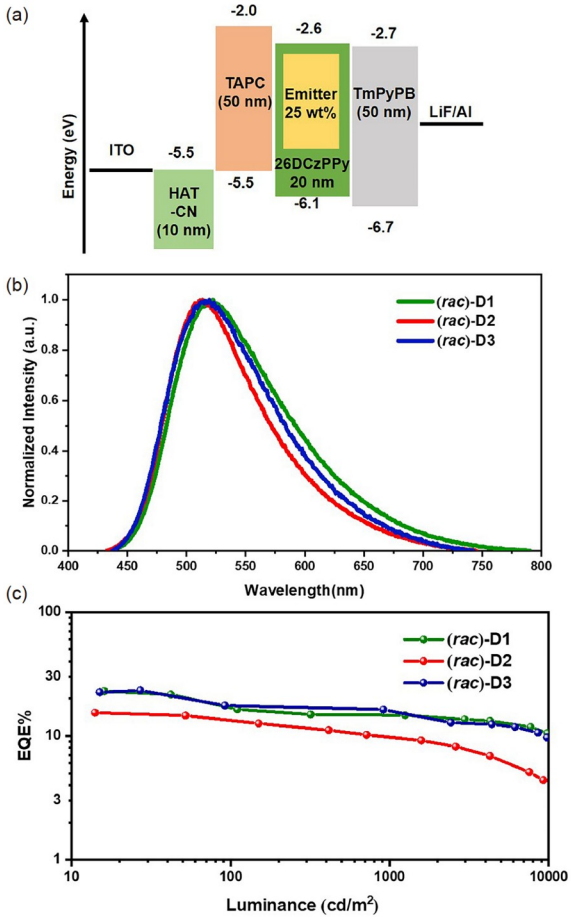

Figure 6 (a) OLED structures and energy diagrams of used materials; (b) electroluminescent spectra at voltage of 6 V; (c) EQE-luminance curves of **D1**, **D2** and **D3** devices (color online).

as high as 23.3%, and the value still can be kept as 16.3% at high luminance of 1,000 cd/m^2, which existed as the top result of OLEDs based on spiro-type molecules (Table S3).

The noticeable device performance of **D1** and **D3** can be explained in several aspects. (1) The SCN and SCFPY process has extremely small ΔE_{ST} below 0.05 eV and high PLQY close to 90%, which indicates fast RISC process and suppressed nonradiative transition. Thus, both S_1 and T_1 excitons can be effectively harvested. (2) Short delayed fluorescence lifetimes below 3 μs are observed, which can help to inhibit S_1-T_1 annihilation (STA) and T_1-T_1 annihila-

Table 2 Collection of device performances of **D1**, **D2**, **D3** and device based on OSFSO as contrast

Device	V_t [a] (V)	λ_{max} [b] (nm)	L_{max} [c] (cd/m^2)	$\eta_{c.max}$ [d] (cd/A)	$\eta_{p.max}$ [e] (lm /W)	$EQE_{max/1000}$ [f] (%)	CIE coordinates
(*rac*)-**D1**	3.9	519	32,673	66.9	46.7	23.0/14.7	(0.34, 0.53)
(*rac*)-**D2**	3.9	512	14,240	45.0	33.6	15.4/9.8	(0.30, 0.52)
(*rac*)-**D3**	4.2	517	24,921	67.5	44.2	23.3/16.3	(0.31, 0.51)
D(OSFSO)[g]	3.3	472	4,766	38.1	21.8	20.0/19.3	(0.16, 0.24)

a) Turn-on voltage recorded at a brightness of 1 cd/m^2. b) Peak of EL spectrum at voltage of 6 V. c) Maximum luminance. d) Maximum current efficiency. e) Maximum power efficiency. f) Maximum external quantum efficiency and EQE at 1000 cd/m^2. g) Device performance of previously reported TADF molecule OSFSO.

tion (TTA). (3) Bipolar 26DCzPPy is employed as the host material. The ability to smoothly transport both holes and electrons helps effectively balance the carrier recombination zone and reduces the carrier accumulation or excitons annihilation. Besides, no emission peak of host material was observed form EL spectra, indicating an efficient host-guest energy transfer process, which further helps reduce energy waste.

Inspired by the remarkable device performances and stable CPL signals, corresponding CP-OLEDs were also fabricated to characterize the CPEL properties of three pairs of enantiomers. As shown in Figure 7, devices (*R*/*S*)-**D1**, (*R*/*S*)-**D2** and (*R*/*S*)-**D3** exhibited almost symmetrical CPEL spectra and the trends were in line with the CPL results of (*R*/*S*)-SCN, (*R*/*S*)-SPHCN and (*R*/*S*)-SCFPY. For (*R*/*S*)-**D1**, the g_{EL} factors were recorded to be $-1.4/1.8\times10^{-3}$ around the maximal emission wavelength. Benefitted from the decreased spatial angel between μ_m and μ_e, (*R*/*S*)-**D2** and (*R*/*S*)-**D3** displayed promoted g_{EL} factors, which were recorded to be $-3.6/3.6\times10^{-3}$ and $-3.7/3.6\times10^{-3}$, respectively. Although the g_{EL} factors of reported CP-OLEDs still remain at 10^{-3} order of magnitude, the g_{EL} of (*R*/*S*)-**D2** and (*R*/*S*)-**D3** is nearly twofold higher than that of (*R*/*S*)-**D1** with the similar chiral skeleton.

4 Conclusions

In conclusion, although tremendous progress has been made in the area of CP-TADF materials, the regulation of CPL property of these molecules remains at the germination stage. In this work, by the systematacially study of three novel TADF enantiomers with similar chiral spiro-skeleton, it is demonstrated that the dissymmetry factor can be amplified more than twofold by simply prolonging the length of acceptor units, which may be attributed to the decrease in spatial angel between μ_m and μ_e. As a result, (*R*/*S*)-SCN enantiomers showed rather low $|g_{PL}|$ factors around 1.4×10^{-3}, while (*R*/*S*)-SPHCN and (*R*/*S*)-SCFPY with extended acceptor units displayed high $|g_{PL}|$ factors of 3.6×10^{-3} and 3.5×10^{-3}, respectively. The $|g_{EL}|$ factors of the CP-OLEDs were recorded to be 1.8×10^{-3}, 3.6×10^{-3} and 3.7×10^{-3} for (*R*/*S*)-**D1**, (*R*/*S*)-**D2** and (*R*/*S*)-**D3**, exhibiting similar trends with that of g_{PL} factors of the enantiomers. Besides, all devices displayed decent performances with green emissions, e.g., EQE_{max} for **D1**, **D2** and **D3** were recorded to be 23.0%, 15.4% and 23.3%. Especially for device **D3** with SCFPY as emitter, EQE_{max} of 23.3% represented a recorded high data among all the reported spiro-type TADF materials. The results indicated that high *g* factors and remarkable device performances can be achieved simultaneously for chiral TADF molecules. This study emphasized the importance of functional group engineering and we believe this work would be instructive in developing CP-TADF materials.

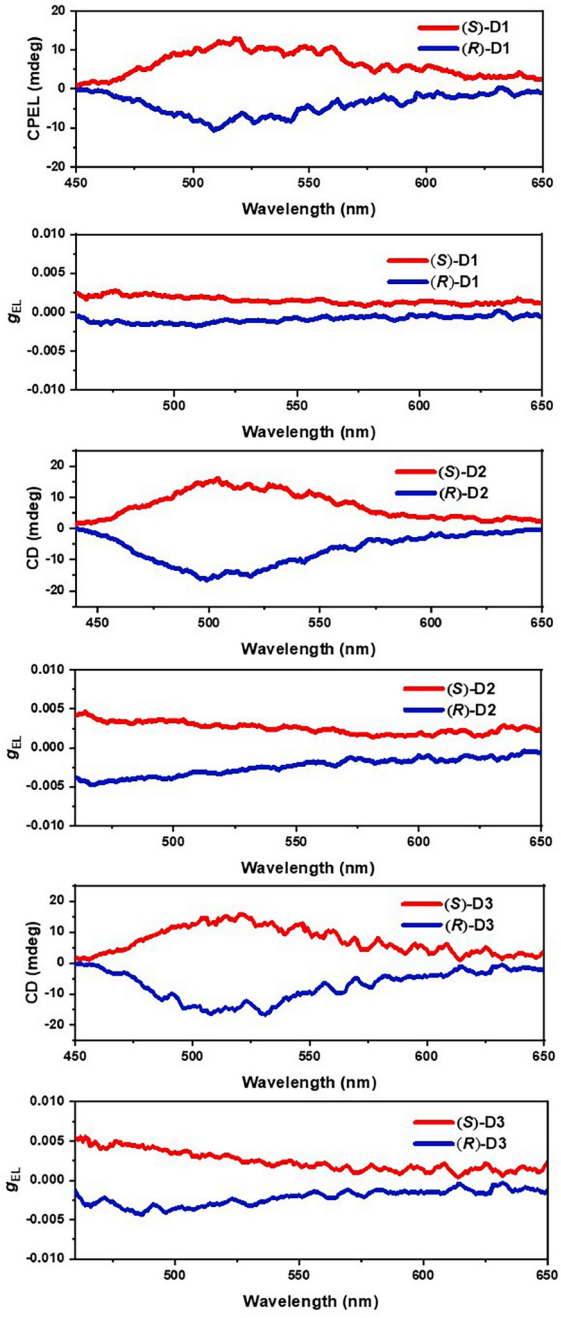

Figure 7 CPEL spectra and g_{EL} *vs*. wavelengh curves of devices (*R*/*S*)-**D1**, (*R*/*S*)-**D2** and (*R*/*S*)-**D3** (color online).

Acknowledgements This work was supported by the National Natural Science Foundation of China (21975119, 51773088).

Conflict of interest The authors declare no conflict of interest.

Supporting information The supporting information is available online at http://chem.scichina.com and http://link.springer.com/journal/11426. The supporting materials are published as submitted, without typesetting or editing. The responsibility for scientific accuracy and content remains entirely with the authors.

1 Sang Y, Han J, Zhao T, Duan P, Liu M. *Adv Mater*, 2020, 32: 1900110
2 Frédéric L, Desmarchelier A, Favereau L, Pieters G. *Adv Funct Mater*, 2021, 31: 2010281
3 Gong ZL, Zhu X, Zhou Z, Zhang SW, Yang D, Zhao B, Zhang YP, Deng J, Cheng Y, Zheng YX, Zang SQ, Kuang H, Duan P, Yuan M, Chen CF, Zhao YS, Zhong YW, Tang BZ, Liu M. *Sci China Chem*, 2021, 64: 2060–2104
4 Tao Y, Yuan K, Chen T, Xu P, Li H, Chen R, Zheng C, Zhang L, Huang W. *Adv Mater*, 2014, 26: 7931–7958
5 Feuillastre S, Pauton M, Gao L, Desmarchelier A, Riives AJ, Prim D, Tondelier D, Geffroy B, Muller G, Clavier G, Pieters G. *J Am Chem Soc*, 2016, 138: 3990–3993
6 Song F, Xu Z, Zhang Q, Zhao Z, Zhang H, Zhao W, Qiu Z, Qi C, Zhang H, Sung HHY, Williams ID, Lam JWY, Zhao Z, Qin A, Ma D, Tang BZ. *Adv Funct Mater*, 2018, 28: 1800051
7 Wu ZG, Han HB, Yan ZP, Luo XF, Wang Y, Zheng YX, Zuo JL, Pan Y. *Adv Mater*, 2019, 31: 1900524
8 Wu ZG, Yan ZP, Luo XF, Yuan L, Liang WQ, Wang Y, Zheng YX, Zuo JL, Pan Y. *J Mater Chem C*, 2019, 7: 7045–7052
9 Sharma N, Spuling E, Mattern CM, Li W, Fuhr O, Tsuchiya Y, Adachi C, Bräse S, Samuel IDW, Zysman-Colman E. *Chem Sci*, 2019, 10: 6689–6696
10 Sun S, Wang J, Chen L, Chen R, Jin J, Chen C, Chen S, Xie G, Zheng C, Huang W. *J Mater Chem C*, 2019, 7: 14511–14516
11 Frédéric L, Desmarchelier A, Plais R, Lavnevich L, Muller G, Villafuerte C, Clavier G, Quesnel E, Racine B, Meunier-Della-Gatta S, Dognon JP, Thuéry P, Crassous J, Favereau L, Pieters G. *Adv Funct Mater*, 2020, 30: 2004838
12 Ni F, Huang CW, Tang Y, Chen Z, Wu Y, Xia S, Cao X, Hsu JH, Lee WK, Zheng K, Huang Z, Wu CC, Yang C. *Mater Horiz*, 2021, 8: 547–555
13 Xu Y, Wang Q, Cai X, Li C, Wang Y. *Adv Mater*, 2021, 33: 2100652
14 Xue P, Wang X, Wang W, Zhang J, Wang Z, Jin J, Zheng C, Li P, Xie G, Chen R. *ACS Appl Mater Interfaces*, 2021, 13: 47826–47834
15 Liao C, Zhang Y, Ye SH, Zheng WH. *ACS Appl Mater Interfaces*, 2021, 13: 25186–25192
16 Xie F, Zhou J, Zeng X, An Z, Li Y, Han D, Duan P, Wu Z, Zheng Y, Tang J. *Adv Opt Mater*, 2021, 9: 2100017
17 Li M, Li SH, Zhang D, Cai M, Duan L, Fung MK, Chen CF. *Angew Chem Int Ed*, 2018, 57: 2889–2893
18 Wang Y, Zhang Y, Hu W, Quan Y, Li Y, Cheng Y. *ACS Appl Mater Interfaces*, 2019, 11: 26165–26173
19 Wang YF, Lu HY, Chen C, Li M, Chen CF. *Org Electron*, 2019, 70: 71–77
20 Li M, Wang YF, Zhang D, Duan L, Chen CF. *Angew Chem Int Ed*, 2020, 59: 3500–3504
21 Wang YF, Li M, Zhao WL, Shen YF, Lu HY, Chen CF. *Chem Commun*, 2020, 56: 9380–9383
22 Tu ZL, Yan ZP, Liang X, Chen L, Wu ZG, Wang Y, Zheng YX, Zuo JL, Pan Y. *Adv Sci*, 2020, 7: 2000804
23 Wang Y, Li M, Teng J, Zhou H, Chen C. *Adv Funct Mater*, 2021, 31: 2106418
24 Tu Z, Lu J, Luo X, Hu J, Li S, Wang Y, Zheng Y, Zuo J, Pan Y. *Adv Opt Mater*, 2021, 9: 2100596
25 Hayashi K, Matsumoto A, Hirata S. *Chem Commun*, 2021, 57: 1738–1741
26 Zhao WL, Wang YF, Wan SP, Lu HY, Li M, Chen CF. *CCS Chem*, 2022, 1–9
27 Zhang YP, Mao MX, Song SQ, Wang Y, Zheng YX, Zuo JL, Pan Y. *Angew Chem Int Ed*, 2022, doi: 10.1002/anie.202200290
28 Imagawa T, Hirata S, Totani K, Watanabe T, Vacha M. *Chem Commun*, 2015, 51: 13268–13271
29 Yang SY, Wang YK, Peng CC, Wu ZG, Yuan S, Yu YJ, Li H, Wang TT, Li HC, Zheng YX, Jiang ZQ, Liao LS. *J Am Chem Soc*, 2020, 142: 17756–17765
30 Zhang YP, Liang X, Luo XF, Song SQ, Li S, Wang Y, Mao ZP, Xu WY, Zheng YX, Zuo JL, Pan Y. *Angew Chem Int Ed*, 2021, 60: 8435–8440
31 Wu X, Huang JW, Su BK, Wang S, Yuan L, Zheng WQ, Zhang H, Zheng YX, Zhu W, Chou PT. *Adv Mater*, 2022, 34: 2105080
32 Li JK, Chen XY, Guo YL, Wang XC, Sue ACH, Cao XY, Wang XY. *J Am Chem Soc*, 2021, 143: 17958–17963
33 Yang SY, Zou SN, Kong FC, Liao XJ, Qu YK, Feng ZQ, Zheng YX, Jiang ZQ, Liao LS. *Chem Commun*, 2021, 57: 11041–11044
34 Yan Z, Liu T, Wu R, Liang X, Li Z, Zhou L, Zheng Y, Zuo J. *Adv Funct Mater*, 2021, 31: 2103875
35 Yang SY, Tian QS, Liao XJ, Wu ZG, Shen WS, Yu YJ, Feng ZQ, Zheng YX, Jiang ZQ, Liao LS. *J Mater Chem C*, 2022, 10: 4393–4401
36 Nakagawa T, Ku SY, Wong KT, Adachi C. *Chem Commun*, 2012, 48: 9580–9582
37 Méhes G, Nomura H, Zhang Q, Nakagawa T, Adachi C. *Angew Chem Int Ed*, 2012, 51: 11311–11315
38 Nasu K, Nakagawa T, Nomura H, Lin CJ, Cheng CH, Tseng MR, Yasuda T, Adachi C. *Chem Commun*, 2013, 49: 10385–10387
39 Ohkuma H, Nakagawa T, Shizu K, Yasuda T, Adachi C. *Chem Lett*, 2014, 43: 1017–1019
40 Wang YK, Wu SF, Yuan Y, Li SH, Fung MK, Liao LS, Jiang ZQ. *Org Lett*, 2017, 19: 3155–3158
41 Rao J, Zhao C, Wang Y, Bai K, Wang S, Ding J, Wang L. *ACS Omega*, 2019, 4: 1861–1867
42 Zhu XD, Peng CC, Kong FC, Yang SY, Li HC, Kumar S, Wang TT, Jiang ZQ, Liao LS. *J Mater Chem C*, 2020, 8: 8579–8584
43 Wang Y, Huang C, Ye H, Zhong C, Khan A, Yang S, Fung M, Jiang Z, Adachi C, Liao L. *Adv Opt Mater*, 2020, 8: 1901150
44 Sharma N, Maciejczyk M, Hall D, Li W, Liégeois V, Beljonne D, Olivier Y, Robertson N, Samuel IDW, Zysman-Colman E. *ACS Appl Mater Interfaces*, 2021, 13: 44628–44640
45 Wang R, Li Z, Hu T, Tian L, Hu X, Liu S, Cao C, Zhu ZL, Tan JH, Yi Y, Wang P, Lee CS, Wang Y. *ACS Appl Mater Interfaces*, 2021, 13: 49066–49075
46 Xie JH, Zhou QL. *Acc Chem Res*, 2008, 41: 581–593
47 Saragi TPI, Spehr T, Siebert A, Fuhrmann-Lieker T, Salbeck J. *Chem Rev*, 2007, 107: 1011–1065
48 Lu T, Chen F. *J Comput Chem*, 2012, 33: 580–592
49 Yang SY, Qu YK, Liao LS, Jiang ZQ, Lee ST. *Adv Mater*, 2021, n/a: 2104125
50 Peng CC, Yang SY, Li HC, Xie GH, Cui LS, Zou SN, Poriel C, Jiang ZQ, Liao LS. *Adv Mater*, 2020, 32: 2003885